ARTICLE   OPEN

Check for updates

Structure--property relationship and chemical durability of magnesium-containing borosilicate glasses with insight from topological constraints

N. Bisbrouck [1], M. Micoulaut[2], J. M. Delaye[1], S. Gin [1] and F. Angeli[1 ✉]

The initial dissolution rate of a series of multicomponent glasses is studied in order to discuss the influence of increasing magnesium content in the glass on this alteration regime and to highlight differences in behavior between calcium- and magnesium-bearing glasses. The application of MD-based topological constraint theory (TCT) is confronted to glass transition temperature (T_g) and initial dissolution rate (r_0) on a glass series containing the main oxides of a French nuclear glass (AVM). In addition, a comparison between a reference magnesium-containing nuclear waste glass, AVMV4 and a proposed derived simplified composition N19M8 is performed regarding r_0 values. Results indicate a similar behavior in this alteration regime for the two glasses, suggesting that this simple glass might be a good analogue to the complex one. Substituting calcium for magnesium decreases the initial dissolution rate by a factor two in the series, while an overall increase of magnesium leads to an increased dissolution rate. Analyses performed with TCT suggests that magnesium environment is better defined than calcium or sodium and may behave as an intermediate species. Finally, a correlation between the number of constraints per atom and T_g is established, while the model failed to link structural features to r_0.

INTRODUCTION

Multi-component silicate glasses have been increasingly used over the years, becoming of such stupendous importance that Morse et al. suggested our era to be referred to as *Glass Age*[1]. Indeed, this vitreous material has found various applications ranging from kitchen or laboratory glassware[2], windows or glass covers[3,4], to high-end technological glasses for medical applications[5–8] or nuclear waste immobilization[9–12]. This wide range of applications is possible accounting for the versatility of glasses, virtually endlessly tailorable to reach a targeted property. However, this can only be achieved through a thorough and deep understanding of the structure–composition–property relationship, which remains difficult to grasp, and becomes even harder with increasing glass complexity. Indeed, variations in composition intrinsically induces changes on the glass structure, and thus its properties, either mechanical properties[13–17], glass transition temperature[5], viscosity[15], and chemical durability[18–21].

Glass alteration is a rather complex phenomenon involving several concurrent and/or successive reactions in aqueous environment[22]. In addition to intrinsic parameters such as glass composition[23] and structure[18], extrinsic parameters such as solution temperature[23–25], pH[26–28] or chemistry[24,29] impact the dissolution process and kinetics. Furthermore, the alteration rate may vary over time, as for borosilicate glasses used for nuclear waste disposal[19]. Consequently, several alteration regimes have thus been evidenced, one of which referred to as forward dissolution rate (r_0) or Stage 1. Mechanistically, this stage is dominated by the hydrolysis of the silicate network, i.e., Si–O–M bond breaking (M a given network-forming cation, such as Si, B, Al...) and corresponds to the maximum alteration rate of the glass under a given temperature and pH conditions. Afterwards, a passivating alteration layer can be formed, leading to a decrease

of the dissolution rate by several orders of magnitude. This alteration regime is called Stage 2 or residual rate. Finally, a resumption of the alteration (or Stage 3) can occur due to the precipitation of secondary phases, consuming the silicon from the alteration layer[11,30–33]. Magnesium can participate in the precipitation of secondary phases when present either as a dissolution product from the glass or initially as part of the solution[11,31–33], but does not contribute to Stage 3.

However, while there has been several studies on the effect of magnesium on the residual rate[11,31,33–38] on simple or industrial glasses for nuclear waste disposal such as Magnox (UK) and AVM (France) glasses, there is a limited amount of data on the impact of magnesium as part of the composition on the initial dissolution rate[10,21,38,39] of such glasses. In addition, the complexity of industrial glasses renders difficult ascribing variation in r_0 measurements with composition. As such, relying on the study of simple glasses has proven to be useful to achieve a better understanding of the alteration mechanisms, as is the case of the International Simple Glass (ISG)[9,19].

In recent years several models emerged linking structural characteristics and various properties of a given material. For instance, topological constraint theory (TCT)[40–43] has demonstrated promising correlations between a number of constraints per atom (n_c) and hardness[44,45], fracture toughness[46,47] or dissolution kinetics under varying conditions[48–53], and has given insight into the origin of complex and peculiar phenomenon such as the mixed-modifier effect[54]. This was made possible through advances made in molecular dynamic (MD) simulations in accurately reproducing the salient features of experimental data.

In this study, following a comprehensive experimental[55] and numerical[56] structural characterization of seven silicate glasses, part of them containing magnesium, initial dissolution rate

[1]CEA, DES, ISEC, DE2D, Université de Montpellier, 30207 Marcoule, Bagnols-sur-Cèze Cedex, France. [2]Laboratoire de Physique Théorique de la Matière Condensée, Sorbonne Université, CNRS UMR 7600, 4 Place Jussieu, 75252 Cedex 05 Paris, France. ✉email: frederic.angeli@cea.fr

N. Bisbrouck et al.

Table 1. Nominal composition of the studied glasses, expressed in molar percent of oxide, alongside associated measured glass transition temperature (T_g), density (ρ) and NMR-extracted fourfold coordinated boron percentage.

Glass ID	Chemical composition (mol%)						T_g (°C)	ρ	B^{IV} (%)[55]
	SiO_2	B_2O_3	Al_2O_3	Na_2O	MgO	CaO			
N26M0	51.3	14.9	7.7	26.1	–	–	523	2.505	57
N19M8	51.2	14.9	7.7	18.7	7.5	–	573	2.45	37
N13M13	51.2	14.9	7.7	13.1	13.1	–	594	2.421	24
N8M19	51.2	14.9	7.7	7.5	18.7	–	642	2.412	7
N0M12	51.3	24.2	12.4	–	12.1	–	703	2.31	2
N19C8	51.2	14.9	7.7	18.7	–	7.5	573	2.511	46
A0B0	66.1	–	–	24.2	9.7	–	495	2.486	–

experiments were performed to evaluate the influence of increasing sodium–magnesium substitution on the chemical durability of borosilicate glasses. One of the glass compositions is based on the five major oxide of the industrial glass AVMV4[11], with a calcium counterpart to investigate the impact of the two alkali-earth on the initial dissolution rate. Dissolution experiments were performed at 90 °C, $pH^{90°C} = 9$ and low glass-surface-area-to-solution-volume ratio to ensure that the alteration process is rate-controlled by the hydrolysis of the network. As such, r_0 measurements are based on the release of Si in the leaching solution. The calculation of n_c was performed on previously validated structure models, allowing an accurate topological constraint enumeration[40], as widely used in other studies on chalcogenide[57,58] and oxide[59–61] glasses.

RESULTS AND DISCUSSION
Experimental results
The composition of the studied glasses is displayed in Table 1, alongside various physico-chemical properties, namely the vitreous transition temperature T_g, density ρ and percentage of fourfold coordinated boron extracted from ^{11}B Nuclear Magnetic Resonance (NMR) in our previous study[55]. All glasses are found to be homogeneous. In the most magnesium-rich (N8M19) glass, two-sub-networks were suggested based on Raman and ^{17}O MQMAS analyses[55]. In addition, calculating the ratio ΣAlcalis/ΣCations reveals that two glasses are above the percolation threshold of 0.31 proposed by Devreux and Kold[62], namely N26M0 and A0B0, with a ratio value of 0.35 and 0.39 respectively. The release of silicon determined from UV-visible spectrophotometry is found to be linear through time for all glasses (see Fig. 1). For most of the glasses, the initial and final pH values remained unchanged within uncertainties, i.e $pH^{90°C} = 9 \pm 0.1$, except for the A0B0 glass for which the pH increased up to 9.4 despite regular addition of nitric acid during the test. This was to be expected considering the high sodium content leading to increased ion-exchange coupled to an absence of boron decreasing the pH.

For each glass, at least one series of experiments was analyzed by ICP-OES, allowing to observe the release of all the elements of the vitreous matrix. The results displayed in Fig. 2 shows that most glasses dissolve congruently within analyses uncertainties, with similar slopes obtained for all elements. The two glasses whose compositions were found to be above the percolation threshold, namely N26M0 and A0B0, dissolve incongruently, with a preferential release of boron and sodium (respectively only sodium) six and ten times faster that the other elements for N26M0 and A0B0, respectively. In both cases the release of sodium (and boron) is not linear and intercepting zero, suggesting that two mechanisms are at stakes: when in contact with the solution, a fast release of boron and sodium occurs, depleting the first nanometers of the glass. Following this depletion, the release of
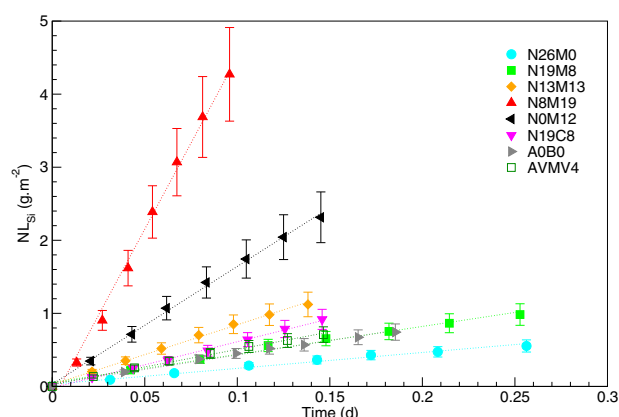

Fig. 1 Time dependence of normalized mass loss (NL) based on Si release obtained at $pH^{90°C} = 9$ and $T = 90$ °C for all the studied glasses. Dashed lines represents the linear regression. Uncertainties on NL based on silicon concentration for a given test are given at ± 15% based on instrumental measurements. Overall uncertainties r_0 determination are given at ± 30%.

these elements becomes partially rate-controlled by the hydrolysis of the vitreous system, but they remain preferentially accessible and released through sodium-rich channels. Interestingly, for A0B0, magnesium is released at the same rate as silicon, which indicates a stronger incorporation of this element into the silicate network. This could be linked to the fact that interactions between magnesium and oxygen atoms are higher than those between sodium and oxygen atoms, or that part of the magnesium is more deeply connected to the vitreous network through low coordination states suggested by ^{25}Mg MAS NMR[55] and MD simulations[56].

Finally, for the magnesium-rich glass N8M19, aluminium and magnesium release are found to be slightly lower than for the other elements, which may be due to the fact that magnesium partly compensates for aluminium in this glass, as observed previously by NMR[55]. However, the discrepancy between the slopes falls within uncertainties.

Altogether, the linear release of silicon (with an intercept close to zero) in highly diluted conditions coupled to congruent dissolution for most of the glasses confirms that experiments were conducted in the initial dissolution regime, and that the measured rates are equivalent to the forward dissolution rate. As such, silicon can be considered as tracer of the alteration, and used for r_0 determination, given in Table 2, which are spanning over one order of magnitude. For the glasses dissolving incongruently, this rate corresponds to the dissolution of the remaining sodium–boron- (respectively sodium-) depleted network, i.e., a relatively rich silicon–aluminium- (respectively silicon-) rich hydrated and potentially reorganized layer.
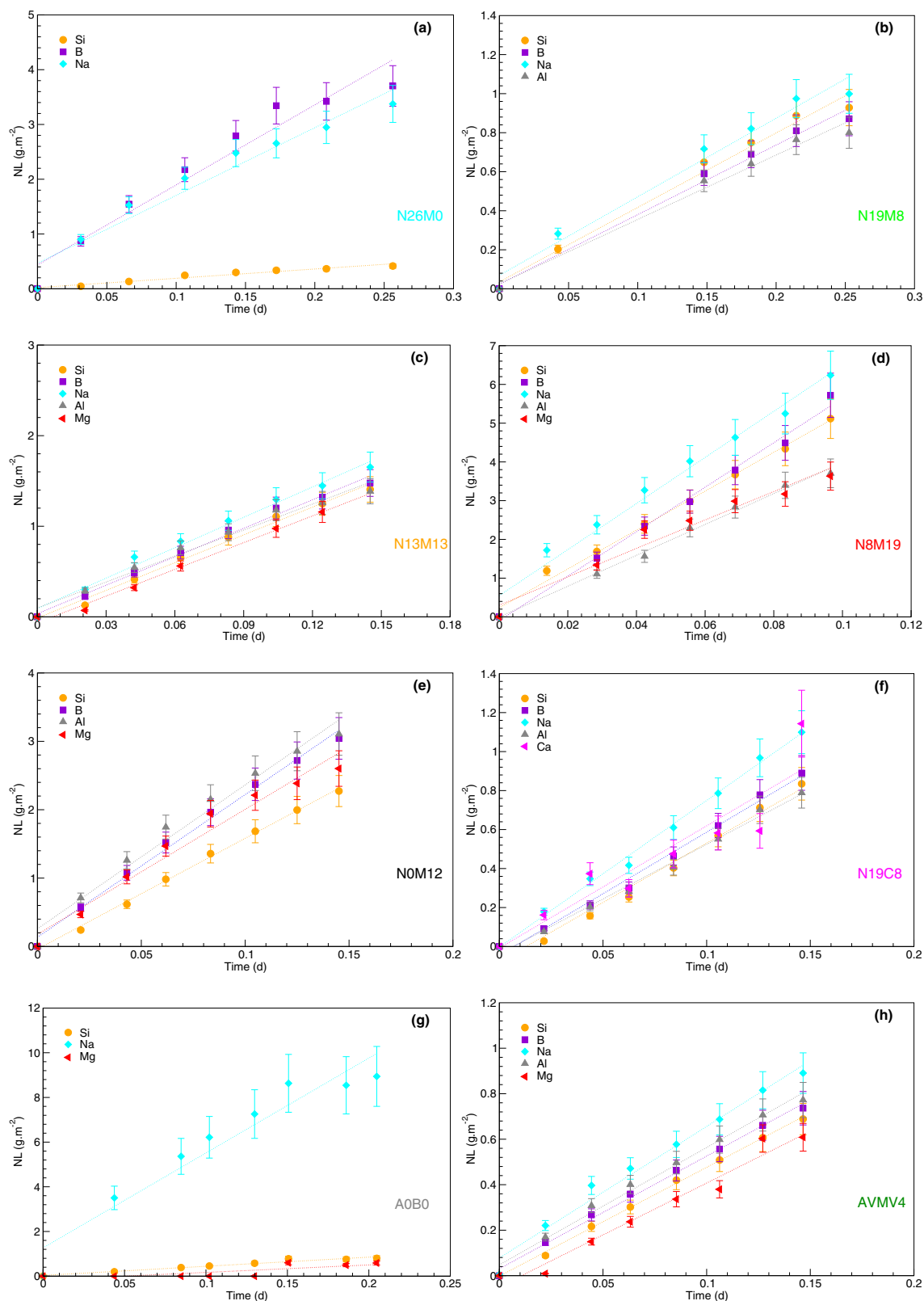
Fig. 2 Evaluation of the congruency of dissolution through ICP-OES-based NL calculation of all elements through time for the different glasses. a N26M0, **b** N19M8, **c** N13M13, **d** N8M19, **e** N0M12, **f** N19C8, **g** A0B0 and **h** AVMV4. Dashed lines represents the linear regression. Uncertainties on NL based on elemental concentration for a given test are given at ± 15% based on instrumental measurements.

Table 2. Parameters of initial dissolution rate r_0 experiments, alongside r_0 values calculated by linear regression based on NL_{Si}. pH values are given with a ± 0.1 uncertainty.

Glass ID	Number of test	Mass of glass (g)	Volume (L)	Glass fraction powder (μm)	Initial S/V (cm^{-1})	r_0 Si (g.m^{-2}.d^{-1})	ln(r_0 Si)	Final pH 90°C
N26M0	11	0.230	0.50	100–125	0.1	3.0 ± 0.9	1.09	8.9
N19M8	8	0.230	0.50	100–125	0.1	3.8 ± 1.1	1.35	9.0
N13M13	5	0.068	0.50	100–125	0.025	7.7 ± 2.3	2.04	9.0
N8M19	11	0.068	1.00	100–125	0.025	48.3 ± 14.5	3.88	9.1
N0M12	11	0.106	0.50	100–125	0.05	15.5 ± 4.7	2.74	8.9
N19C8	9	0.230	0.50	100–125	0.1	6.7 ± 2	1.91	9.0
A0B0	4	0.230	0.50	100–125	0.1	4.1 ± 1.3	1.43	9.4
AVMV4	1	0.106	0.50	40–63	0.1	4.8 ± 1.4	1.56	9.1

This is the case for the N26M0 glass, which does not contain magnesium. The r_0 measurement based on silicon release indicates a value of 3 g m^{-2} d^{-1}, while based on boron release from ICP-OES this value reaches 18 g m^{-2} d^{-1}. As such, we can hypothesize that if the glass was to be macroscopically homogeneous, the obtained r_0 would be in-between these two values, which here results in an underestimated apparent dissolution. It is important to highlight the fact the incongruency of dissolution of the sodium-rich glass renders difficult to assess primarily and only the role of sodium–magnesium substitution.

Substituting 7.5 mol% Na$_2$O by CaO, i.e., from N26M0 to N19C8, results in an increase in the dissolution rate by factor two, reaching 6.7 g m^{-2} d^{-1}. This increase might be partially related to the increase in the fraction of B^{III} and as a consequence the number of NBOs[55,56], favouring the dissolution[18,63–65] compared to the N26M0 glass. However, these structural modifications might be of secondary importance: totally substituting calcium for magnesium results in a further increase in NBO and tri-coordinated boron[55,56], but a decrease in r_0 is observed, reaching 3.8 g m^{-2} d^{-1}, which is slightly higher than for the N26M0 glass but falls within uncertainties.

Increasing further the sodium–magnesium substitution to 13.1 mol% of MgO (N13M13) leads to an increase of the r_0 value to 7.7 g m^{-2} d^{-1}. Interestingly, this value is quite close to that of the calcium-containing glass (N19C8), which could indicate that for a given number of calcium atom, a higher number of magnesium atoms is needed to generate the same impact on the dissolution rate, which highlight the distinctive role of magnesium compared to calcium. Again, increasing magnesium content lead to a further increase in both NBOs and B^{III} units, which confirms that these structural modifications are of second-order regarding the variation of the dissolution rate.

Finally, in the series, reaching 18.7 mol% of MgO drastically increases the initial dissolution rate, with an increase to 48.3 g m^{-2} d^{-1}, i.e an increase by a factor six compared to the N13M13. Previously obtained structural information[55] may partly explain this phenomenon, as it was evidenced that magnesium atoms generated more boroxol ring structure, easier to dissolve[64–66], up to the point where a phase-separation in two sub-network was observed for the N8M19 glass[55]. In addition, this glass contains the highest B^{III} and NBO content of sodium–magnesium substitution glass series. Altogether, increasing magnesium content at the expense of sodium appears to increase the initial dissolution rate along this series, but due to the various structural changes induced by a single elemental substitution (sodium for magnesium), it remains difficult to assess which modification is primarily responsible for the overall increase in r_0.

The industrial-like glass AVMV4 is found to dissolve at a similar rate, within uncertainties, as its derivate of simpler composition N19M8 ($r_0 = 3.8$ g m^{-2} d^{-1} and 4.8 g m^{-2} d^{-1} respectively). This result suggests that it is reasonable to assume that N19M8 is a

good candidate to better understand far more complex glasses like the AVMV4, in the same way the ISG glass is used as a model for the SON68 glass[19]. As such, structure–composition–properties relationships evidenced here might be applicable for the industrial composition to some extent. The case of the N0M12 and A0B0 glasses is peculiar, as the compositions were designed as references for structural analyses but deviate from the systematic substitution that was applied for the rest of the glass series. It is therefore more difficult to ascribe the structural changes observed to the measured dissolution rate in a comparative study. As above-mentioned, the magnesium containing glass N19M8 dissolves two times slower than its calcium counterpart N19C8, which indicates that magnesium strengthen the vitreous network to some extent and may endorse an intermediate role in the glass as suggested in several studies[21,67–69]. This is usually attributed to magnesium in low coordination states, i.e., tetrahedral units, which has been suggested in the series in our previous NMR[55] and MD[56] studies. While some discrepancies between experimental and numerical glass structure were previously observed, which could result in variations of the enumeration of topological constraints, the latter is used to decipher the peculiar role of magnesium in the series through a complementary structural study.

TCT model and calculation

The number of constraints per atom n_c was calculated using numerical simulations by enumerating bond-stretching (BS) and bond-bending (BB) constraints generated by each type of atomic species. While several type of materials[40,44,48,60,70,71], thus elements, have been investigated in the past, there is no data available regarding the MD-obtained topological constraints induced by magnesium to the best of our knowledge. Silicon and tetrahedral aluminium atoms are usually found to generate four BS and five BB constraints, which is consistent with their respective coordination number[48,49,60,72,73]. The covalent nature of their bonds allows for both relatively small radial σ_r and angular σ_θ excursion. In a similar way, tri-coordinated boron are known to generate $n_c^{BS}(B^{III}) = 3$ BS and $n_c^{BB}(B^{III}) = 3$ BB constraints[51,53], while the case of tetrahedral boron is subject to more discussions. It is generally admitted that fourfold coordinated boron generates $n_c^{BS}(B^{III}) = 4$ BS constraints, however the enumeration of BB constraints differs depending on the studies, from usually five[51] (respective of the tetrahedron and consistent with other fourfold coordinated network-former) to none[53] (considering that the angular constraints are destabilized by the need to charge compensate). While the number of constraints generated by network-forming species is usually consistent with their coordination numbers, those induced by network-modifiers can also greatly vary depending on the composition of the studied system. Calcium atoms were suggested to generate from two to slightly over three BS constraints[53,60], whereas sodium atoms are usually
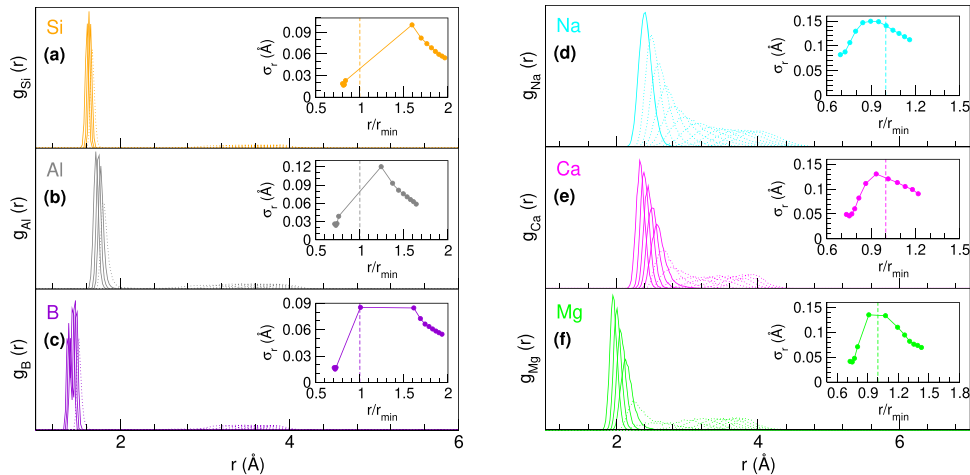
Fig. 3 Partial pair correlation function for the different cations and their 12 nearest neighbors in the N19M8 glass, with addition of calcium contribution from N19C8 as a comparison. a–f Refer to Si, Al, B, Na, Ca and Mg environment respectively. Dashed lines correspond to a large distribution of environments. Insets display the mean radial excursion value of the 12 nearest neighbors as a function of their distance to the considered element, rescaled by the minimum value of the partial pair correlation r_{min}. Dashed lines in insets allow to distinguish first (<1) and second (>1) shell of neighbor.
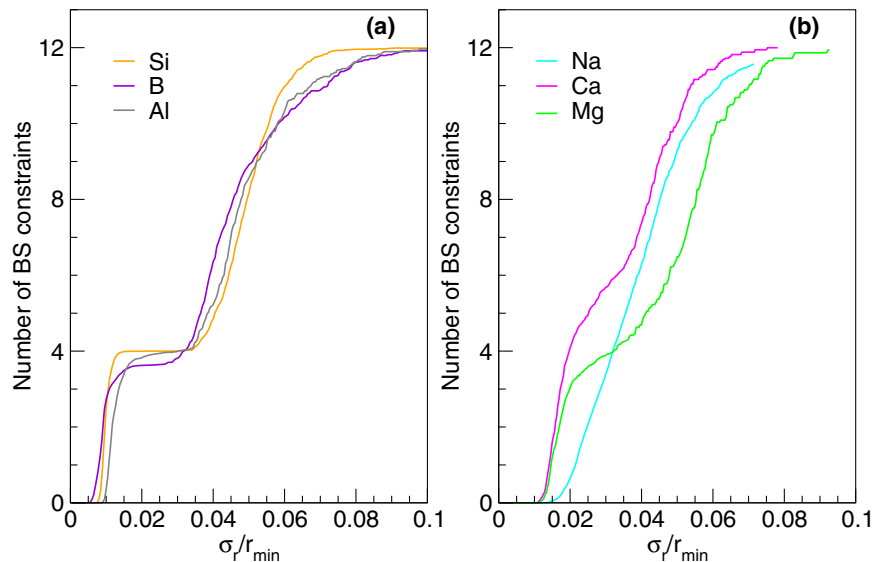

Fig. 4 Number of BS constraints for the different species in the N19M8 glass, with addition from Ca contribution from the N19C8 glass, as a function of a rescaled radial standard deviation. a Displays network formers while **b** displays network modifier. The values r_{min} are derived from the corresponding minimum of each partial pair correlation function reported elsewhere[56].

considered to generate between one and two BS constraints[53,60], requiring an accurate enumeration based on MD simulations. However, their angular environments being highly distributed, no BB constraints are usually associated with these modifiers.

BS constraints. Individual partial pair correlation functions were evaluated for a given element with its $N = 12$ nearest neighbors (Fig. 3), allowing for the local determination of a mean radial excursion between the considered elements and the nth closest atom, as displayed in the inset, together with separated contributions from first and second shell of atoms. In addition, the number of BS constraints per element was determined based on the evolution of the number of BS constraints as a function of σ_r, as displayed on Fig. 4 for the N19M8 glass, with complementary contribution rising from calcium for the N19C8 glass. In order to better compare the behavior of the different elements, values of the radial excursion were rescaled based on the cut-off value used in a previous study[56].

Partial pair correlation functions for silicon atoms indicates that their average environments are well-defined regarding the four closest neighbors, as expected from the tetrahedral geometry of silicon surrounded by four oxygen atoms. This induces a really small radial excursion ($\sigma_{BS} < 0.03$ Å) which drastically increases for atoms beyond the first coordination shell. As a result, the evolution of the number of BS constraints with increasing σ_r displays a well-defined plateau, which unambiguously yields $n_c^{BS}(\text{Si}) = 4$ in the glass, as usually observed[45,53,60,74]. The value of σ_r used in this study to determine active and broken constraints is determined at the inflection point of the observed plateau, here $\sigma_r = 0.054$ Å for silicon. Similar observations are made for aluminium atoms, which are mainly tetra-coordinated, thus $n_c^{BS}(\text{Al}) = 4$ which also manifests by a well-defined plateau (Fig. 4a) and an associated radial excursion value $\sigma_r = 0.064$ Å. In the case of boron, the number of mean BS constraints is consistent with its mean coordination number, considering $n_c^{BS}(\text{B}^{\text{III}}) = 3$ and $n_c^{BS}(\text{B}^{\text{IV}}) = 4$ by taking a radial
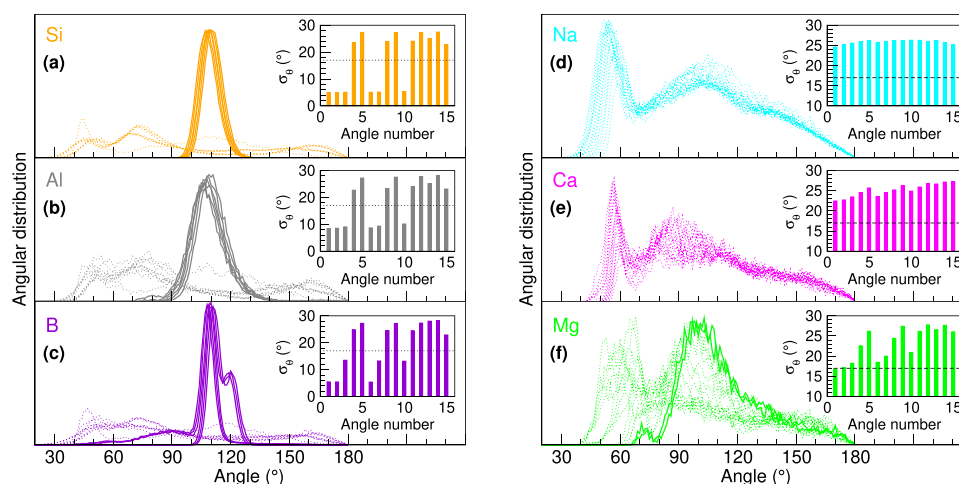
Fig. 5 Angles around the different cations, defined by $N = 6$ first neighbors, i.e., 15 possible bond angle distributions, in the N19M8 glass, with addition of calcium contribution from N19C8 as a comparison. **a–f** Refer to Si, Al, B, Na, Ca and Mg environment respectively. Dashed lines correspond to a large distribution of environments. Insets display the angular excursion relative to each of the 15 angles for a given element. Broken horizontal lines in the insets correspond to an approximate limit (17°) between active and broken angular constraints defined based on literature[74].

excursion value $\sigma_r = 0.046$ Å. It is important to highlight that thanks to the well-defined plateau displayed for the network-forming species, variation of σ_r values do not change significantly the number of enumerated BS constraints.

Regarding sodium atoms, partial pair correlation functions are overall wider than for network-forming species. As such, even the first neighbor mean radial excursion is relatively high. Further analysis indicates a linear increase in BS constraints with increasing σ_r (Fig. 4b), suggesting an overall loosely defined constraints and widely distributed environment. As no plateau can be defined, it is supposed that very few constraints are associated with sodium atoms so that $n_c^{BS}(Na)$ can be considered as negligibly small.

In order to perform a meaningful analysis of the differences between calcium and magnesium environments and their associated constraints, data compared herein are relative to the N19C8 glass for calcium and N19M8 glass for magnesium. Partial PDFs indicates that calcium environment is slightly more ordered than sodium, yet quite distributed as it follows a similar evolution. As one can see on the inset of Fig. 3f, the mean radial excursion value of the four closest neighbors of Mg is indeed relatively low ($\sigma_r < 0.04$ Å), and increases with each additional neighbor. The number of BS constraints associated to calcium atoms displays a plateau-like behavior, despite being less defined than for network-formers (Fig. 4b). In this case, the inflection point allows for the enumeration of the BS constraints with a radial excursion value of $\sigma_r = 0.096$ for Ca, leading to $n_c^{BS}(Ca) = 5.68$ which is lower than the anticipated value expected from the usual count $n^{BS} = r/2$ obtained from a r-coordinated atom, or in this study $n_c^{BS} = r$ as the number of BS on oxygen atoms is not expressed.

Based on the partial PDFs, the environment of magnesium atom appears to be more ordered than calcium as highlighted by the inset in Fig. 3, which shows similar behavior between magnesium and the network-forming species like boron with low radial excursion values for the first three to four closest neighbors located at $\sigma_r \simeq 0.04$ Å. Similarly, $n_c^{BS}(Mg)$ displays a more reduced change with σ_r/r_{min} (Fig. 4b) compared to Na and Ca, albeit not reproducing a plateau behavior typical of Si, Al or B (Fig. 4a). This may suggest that magnesium should be, at least partially, considered as an intermediate between modifier and network-forming species. Calculation of the inflection point of the plateau renders a value of $\sigma_r = 0.088$ for Mg. While this value is the same for all magnesium-containing glasses, the resulting number of constraints per atom is not identical: this point is to be addressed later in the manuscript.

BB constraints. In a similar fashion, the angular excursion of a given element with its $N = 6$ nearest-neighbor, resulting in a total of $N(N - 1)/2 = 15$ possible angles, has been computed for all glasses. Results for the N19M8 glass of the 15 corresponding bond angle distributions per element are displayed in Fig. 5, together with their respective angular excursion per considered angle (insets). Note that panel e of Fig. 5 on calcium originate from the isochemical N19C8 glass.

For the case of silicon-centered bond angles, six over fifteen angles are considered as rigid and display small angular excursions ($\sigma_\theta < 5°$), which again is consistent with the tetrahedral geometry of silicon with four oxygen atoms, yielding a well-defined O–Si–O value of 109°. Note that only five angles are independent. Similar conclusion are drawn regarding aluminium atoms which display a somewhat increased angular excursion ($\sigma_\theta \approx 10°$), and this results in the same number of independent angular constraints $n_c^{BB}(Al) = 5$. For the case of boron, three BB constraints are associated to tri-coordinated boron units (angles 1, 2, 6 in the inset), and fourfold coordinated units display, indeed, five BB constraints in the present systems, as previously hypothesized.

As evidenced in Fig. 5d, no angular constraints are obviously associated with sodium atoms as the latter display a broad bond angle distribution for all 15 angles, the sharp peaks at 40° corresponding to hard-core repulsion that should not be considered. As a result, the angular excursion value for all angles is $\sigma_\theta \approx 25°$, which is larger than the limit for broken constraints. Similarly, a wide distribution of angular environments around calcium is observed in the N19C8 glass, with mean angular excursion found between 22° and 26°, resulting in no angular constraints and suggesting that calcium behaves, indeed, as a network modifier. These findings are globally compatible with the conclusions established for the soda-lime silicate[60] which showed that both Na and Ca were constraining the network only with BS interactions, the corresponding angles displaying distributions similar to those obtained in the present system (Fig. 5d,e).

Conversely, the angular environment around magnesium atoms appears to be intermediate between the features noticed for network-formers (small σ_θ for select rigid angles) and modifiers (all angular constraints broken). While certain angles display, indeed a broad distribution as Na or Ca, certain bond angle distributions appear to be significantly narrower, which suggest a better defined geometry around magnesium. From the analysis, this feature manifests by the presence of at least two angles (inset of Fig. 5f)
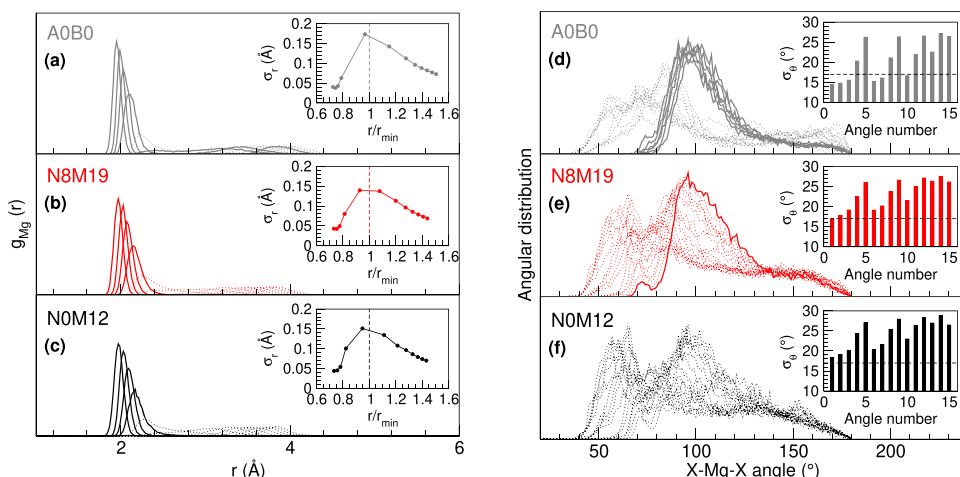
Fig. 6 Comparison of the radial and angular environment around magnesium for three different type of magnesium-containing glasses. Dashed lines correspond to a large distribution of environments. Insets (**a–c**) display the mean radial excursion value of the 12 nearest neighbors as a function of a their distance to the considered element, rescaled by the minimum value of the partial pair correlation r_{min}, while inset for (**d–f**) corresponds to angular excursion relative to each of the 15 angles for a given element. Dashed lines in insets correspond to the limit between active and broken angular constraints, as based on literature.

having a standard deviation σ_θ that is lower than the reported limit between broken and active constraints in such silicates[74]. Similarly to the analysis of the BS constraints, it appears that the number of angular constraints associated with magnesium varies in the glass series, and this is discussed next.

Evolution of magnesium constraints in the series. As introduced earlier, the number of bond stretching constraints associated with magnesium atoms differ from one system to another. Figure 6 indicates that increasing magnesium content in the series only induces slight variations in the enumeration of BS and BB constraints. The mean radial excursion value of the four closest atom appears to be similar, which is confirmed when the evolution of the number of BS constraints with increasing radial excursion is represented (insets of Fig. 6a–c), and this leads to a nearly identical number of BS constraints for N19M8, N13M13 and N8M19. As the base glass A0B0 is examined, one notices however that the mean radial excursion values of the four closest atoms appears to be the lowest of all magnesium-containing glasses ($\sigma_r < 0.06$ Å), with slightly sharper partial PDFs. The inset of Fig. 6 indicates, indeed, that the fourth neighboring atom around magnesium displays smaller radial excursions with respect to the other compositions. Furthermore, one acknowledges the same important increase of σ_r between the fourth and the fifth closest neighbor that has been previously identified for the network-forming species (Fig. 3a–c). Furthermore, for this glass A0B0, the obtained plateau (Fig. 7) is the steepest of the glass series, and might indicate that magnesium partly endorse an intermediate role in the series, and more particularly for A0B0. However, the mean number of BS constraints, associated with magnesium does not differ significantly compared to the three aforementioned glasses (N19M8, N13M13, and N8M19), while for the sodium-free glass N0M12, somewhat fewer constraints are generated. This result indicates that when magnesium is acting as the only charge-compensator, fewer constraints are generated but its environment is more defined than for calcium or sodium.

More striking differences are revealed when the evolution of the angular behavior of magnesium along the series is considered. Increasing magnesium content from N19M8 to N8M19 appears to decrease the number of associated BB constraints : the bond angle distribution is wider which is reflected in the increasing value of the mean angular excursion for all considered angles. While the widest distribution and highest angular excursion value regarding magnesium among all the glasses is attributed to the
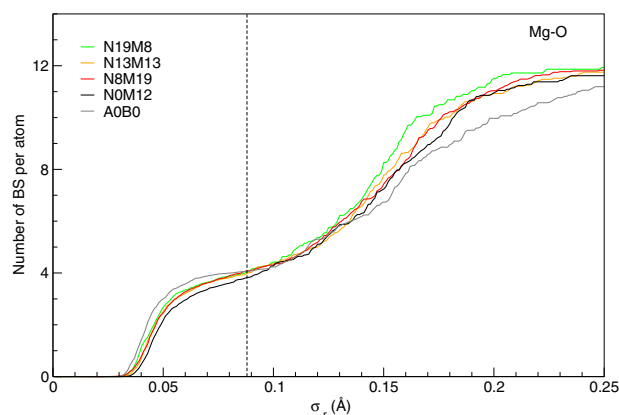

Fig. 7 Number of BS constraints for magnesium in the different glasses, as a function of radial excursion. Dashed lines correspond to the threshold values for the enumeration of the constraints.

sodium-free glass N0M12, the number of BB constraints is similar to the N8M19 glass. As suggested by the results obtained on BS constraints, this may be linked to magnesium increasingly acting as a charge-compensator, thus displaying an overall more distributed environment. Conversely, as observed in the ternary silicate A0B0 when enumerating BS constraints, the bond angle distribution is significantly narrower in this glass, with obvious six rigid angles (inset of Fig. 6d). While their corresponding standard deviation is about $\sigma_\theta \simeq 15°$, the profile of σ_θ with angle number clearly mimics the one observed for network-forming species (Fig. 5a–c). On the overall, it appears from the results that the main variations in the enumeration n_c of the constraints originates from the angular environment of magnesium, whereas BS contributions are independent of composition effect. The number of BS and BB constraints associated to each element depending on glass composition is given in Table 3.

TCT–properties correlation. As the detailed enumeration of constraints per atom has been established, possible correlations between n_c and measured properties such as glass transition temperature or initial dissolution rate were tested out. A clear linear correlation is observed with respect to the T_g (Fig. 8) for the studied glasses: the more constrained a glass is, the higher its glass

Table 3. Number of BS and BB constraints per element for all glasses depending on their composition.

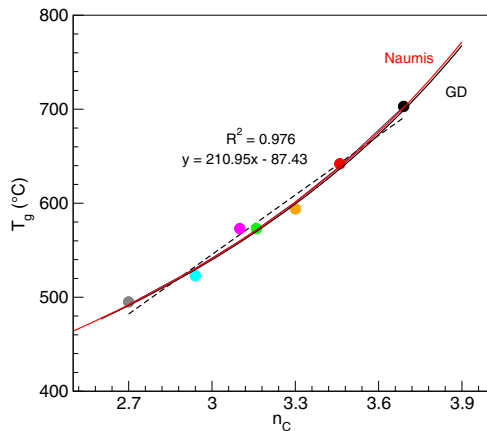| Glass ID	Bond Stretching							Bond Bending							
	Si	B^{III}	B^{IV}	Al	Na	Mg	Ca	Si	B^{III}	B^{IV}	Al	Na	Mg	Ca	O
N26M0	4	3	4	4	–	–	–	5	3	5	5	–	–	–	0.94
N19M8	4	3	4	4	–	4.04	–	5	3	5	5	–	1.43	–	1.09
N13M13	4	3	4	4	–	3.99	–	5	3	5	5	–	1.41	–	1.15
N8M19	4	3	4	4	–	4.07	–	5	3	5	5	–	1.08	–	1.23
N0M12	4	3	4	4	–	3.82	–	5	3	5	5	–	1.17	–	1.31
N19C8	4	3	4	4	–	–	5.68	5	3	5	5	–	–	–	0.94
A0B0	4	–	–	–	–	4.04	–	5	–	–	–	–	1.95	–	0.79

Fig. 8 Glass transition temperature for the seven simple glasses as a function of the number of constraint per atom n_c, averaged on all elements. The broken line is a linear fit to the data, the solid line is a GD[76] fit yielding $T_g(n_c = 2) = 406$ K and $\beta = 0.62$. The red curve is a fit from Naumis model[77]. Colors attributed to each point corresponds to each glass as used in Fig. 1.

Fig. 9 Silicon-based $ln(r_0)$ for the seven simple glasses as a function of the number of constraint per atom n_c, averaged on all elements. Inset displays the evolution of silicon-based $ln(r_0)$ as a function of NBOs. Colors attributed to each point corresponds to each glass as used in Fig. 1.

transition temperature. This result is consistent to some extent with observation made on binary alkali borate by Mauro et al.[75] considering that a different calculation methods was used, and suggests a good enumeration of the constraints for the different elements. It also highlights the general observation that the glass transition temperature is an increasing function of the network connectivity which is proportional to network rigidity (or constraint density n_c). For more simple glasses such as network-forming chalcogenides, such a correlation has been established from a modified Gibbs–Dimarzio (GD) equation[76] which scales as [Eq. 1]:

$$T_g = \frac{T_g(\bar{r} = 2)}{1 - \beta(\bar{r} - 2)} = \frac{5T_g(n_c = 2)}{5 - 2\beta(n_c - 2)} \quad (1)$$

if the mean-field condition[70] $\bar{r} = (2n_c + 6)/5$ is assumed, with $\bar{r}$ corresponding to the mean coordination of the network. Alternatively, Naumis[77] has determined from a more general ground (Lindemann criterion of solidification) a relationship predicting the variation of the glass transition temperature with constraint density. These analytical models are helpful in understanding the effect of composition on T_g, and emphasize the central role played by network connectivity. Furthermore, it highlights the necessity to use MDs simulations to render the variation with composition of n_c based on network-modifiers and charge-compensators, as network-formers usually display constraints based on their coordination number, and provides additional information to help discussing the role of a given element in the glass.

However, while a relatively good correlation has been observed for different glasses between the initial dissolution rate and the
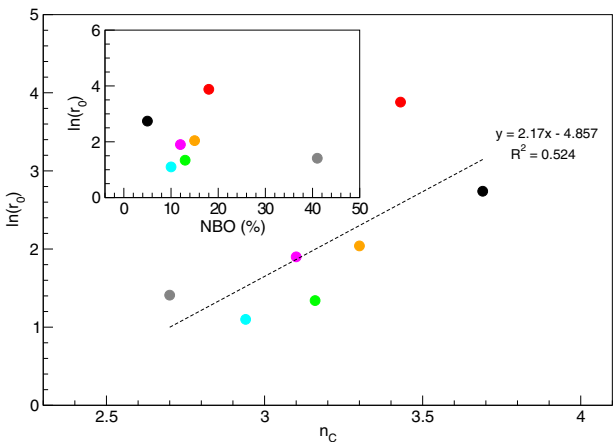
number of constraints per atom in several studies, the present systems do not seem to lead to a similar obvious correlation (Fig. 9) that intuitively suggests that a more constrained glass will dissolve more slowly. There are nonetheless several factors that might explain this unexpected trend when investigating correlation with the reactivity of the glass, as well as the tremendous discrepancy observed here, even when calculating n_c differently based on a more simple model[53] as displayed in Fig. 10. In the TCT approach, no difference is made between a fourfold coordinated aluminium or boron and silicon, who generates the same number of constraints whereas the presence of aluminium or boron in the glass impacts glass durability when substituted for silicon. Recent MDs studies coupled with potential mean force calculations[78] showed that the presence of aluminium as a second neighbor of silicon increased the energy barrier to dissociate bonds when small concentrations of aluminium are present in the glass, while in high concentration it weakens the silicate network. Moreover, it has been showed in a previous study[53] that when glasses are displaying peculiar behavior such as percolation or the presence of sub-networks, which translates to inhomogeneities or incongruent dissolution, the TCT approach could not describe such subtle features : this is confirmed in this study as no percolation channel nor sub-networks were observed in the simulations. As such, it is possible that structural changes observed when increasing magnesium content (increase in boroxol rings for instance), not discriminated by the TCT model, are more important and generates higher reactivity differences in the series than in other glasses, as in Gin et al. study[53]. A more accurate structural description of the glass by MDs may provide a better enumeration of the number of constraints.
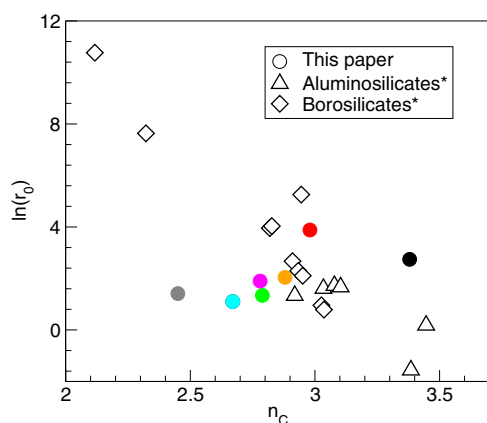
Fig. 10 Silicon-based ln (r_0) for different glasses as a function of n_c, averaged on all elements. n_c is here calculated based on work performed by Gin et al.[53] with asterisks (*) near the glasses type in the legend denoting data obtained in similar conditions from said paper. Colors attributed to each point corresponds to each glass as used in Fig. 1.

In summary, in the studied glasses and conditions, adding magnesium in rather small proportions appeared to increase the chemical durability of glasses in the initial dissolution regime, by a factor two compared to calcium. In addition, the simple five-oxide glass N19M8 displays similar dissolution behavior with the reference nuclear glass on which it is based, the AVMV4, as well as as a decrease in boron coordination coupled to an increase in NBO concentration. Further increase in magnesium however induces drastic structural modifications leading to an increase in the initial dissolution rate, which could also be linked to a modification of the role of magnesium, from intermediate to network-modifier. Application of the TCT model and constraint enumeration strengthen this hypothesis, additionally highlighting the major differences between the environment of calcium and magnesium. However, while good correlations were obtained regarding the glass transition temperature with the number of constraints, no correlation could be made regarding the initial dissolution rate, which suggests that further improvement is needed to refine the model to take into account the influence of the nature of the cation on the glass chemical durability.

METHODS

Glasses composition
The seven silicate glasses studied herein were subject to prior extensive structural characterization, by both experimental[55] and computational means[56]. As such, detailed synthesis and sample preparation is reported elsewhere. Glasses were prepared from a mix of analytical grade oxides and carbonates, and followed a classical melt-quench route. A second fusion was performed to ensure a better homogeneity of the glasses, which was followed by a 1.5 h annealing step at $T_g + 20\,°C$. Powders were obtained by successive grinding, sieving, and ultrasonic cleaning in both acetone and ethanol. Composition were analyzed both by inductively coupled plasma optical emission spectroscopy (ICP-OES) after acid dissolution ($HCl + HNO_3 + HF$) and using an electron probe microanalyzer at the Camparis facility, which ensured the homogeneity of the glasses at the micrometer scale. In addition, transmission electron microscopy (TEM) observations were performed to ensure the absence of nanometre-scale crystallization. All names and compositions are given in Table 1, N and M represent the nominal rounded concentration (mol%) of Na_2O and MgO, respectively. Four of the compositions (N26M0, N19M8, N13M13, and N8M19) aimed to better understand the role of increasing magnesium content on the structure and leaching behavior of these glasses by maintaining a Si/Al and Si/B ratio constant. In addition, a calcium containing counterpart to N19M8, namely N19C8, allowed for a direct comparison between the effect of the two alkaline earth. Glass transition temperature T_g was determined with a SETARAM SETSYS TMA

S60/58507 operating in differential scanning calorimetry mode under an argon atmosphere. Density measurements were carried out by hydrostatic weighting.

Glass alteration
The initial dissolution rate r_0 experiments of each glass were conducted in static mode at 90 °C and $pH^{90°C} = 9$. The onset solution was prepared with 18.2 MΩ cm deionized water heated in an oven to 90 °C ± 3 °C, adjusted with addition of LiOH 1 M to reach a pH value of 9 ± 0.1. In these conditions, the glass dissolution is governed by the hydrolysis of the silicate network through covalent bonds[22,79–81] (e.g., Si–O–M, M = Si, Al or B), allowing for the use of Si to calculate the dissolution rate. 100–125 μm and 40–63 μm powder fractions were used for all of the experiments, and the geometric surface S_{geo} was determined as follow [Eq. 2]:

$$S_{geo} = \frac{6}{\rho \varnothing_m} \qquad (2)$$

with ρ the glass density, and $\varnothing_m$ the mean diameter of the glass powder. This estimation of the surface area of glass powder was used previously and demonstrated a fair approximation of the surface[53,82].

To achieve and maintain the initial dissolution regime, the glass-surface-to-solution-volume ratio S/V has to be low enough to prevent retroaction from dissolved silica on the glass, which would result in a decrease of the alteration rate. Hence, preliminary experiments allowed for the determination of an initial value in the range 0.03 cm^{-1} < S/V < 0.1 cm^{-1}. Experiments were conducted in 500–1000 mL perfluoroalcoxy (PFA) vessels inside of which a 3–5 cm long magnetic bar is introduced, thus maintaining the powder in suspension through the experiment. Several 5 mL samples, respectively 1 mL for inductively coupled plasma-optical emission spectroscopy (ICP-OES) analyses, were taken at regular intervals with a 5 mL syringe, filtrated at 0.45 μm and the S/V variations were reported to be taken into account when calculating the dissolution rate. Regarding that matter, Si concentration was determined by colorimetry, using a Cary Varian UV-visible spectrophotometer at a wavelength of 820 nm and Merck Spectroquant kit, resulting in an accessible concentration range of 0.05–5 mg L^{-1}. ICP-OES analyses, performed on a Thermo Scientific ICAP 6300 Duo, allowed for both a confirmation of the obtained UV-visible Si concentrations and the acquisition of data on other elements, giving insight into the congruency of the dissolution process. Normalized mass loss were then calculated following equation (3):

$$NL_{Si} = \frac{[Si]}{x_{Si}.S/V} \qquad (3)$$

with [Si] the concentration of Si at a time t, x_{Si} the mass fraction of Si in the glass and S/V the glass-surface-to-solution-volume ratio. NL_{Si} is expressed in g.m^{-2}. The linear regression of the evolution of NL_{Si} through time gives access to the initial dissolution rate r_0, expressed in g.m^{-2}.d^{-1} as follows [Eq. 4]:

$$r_0 = \frac{dNL_{Si}}{dt} \qquad (4)$$

Uncertainties on r_0 were estimated based on the work performed by Fournier et al.[82], resulting in a ± 30% upper uncertainties accounting for both reproductibility and error propagation.

Simulation methods
MD simulations used for the constraints enumeration were performed with the LAMMPS package[83] using Wang et al.[84] Coulomb–Buckingham-type interatomic potential, as detailed in a previous study[56]. A summary of the protocol followed for the simulations is found therein. 5000-atom cubic boxes were simulated with respect to the experimentally measured density (Table 1 and reported elsewhere[55]), using periodic boundary conditions. Short- and long-range interactions were defined with a cut-off value of 10 Å. An Ewald summation with a defined accuracy of 10^{-5} was performed. For all simulations, performed in the NVT ensemble (i.e., constant number of atoms, volume, and temperature), a 1 fs timestep was applied. A first equilibration step was performed for 0.1 ps at 1000 K, which allows the removal of the most energetic interactions. The systems were then heated to 3000 K during 1 ns, ensuring a total loss of the initial configuration. Afterwards, the systems were quenched at a 2 K/ps rate to 300 K. Two successive 20 ps equilibration steps were finally performed, firstly in the canonical ensemble, then in the microcanonical NVE ensemble (i.e., constant number of atoms, volume, and energy).

Topological constraints enumeration

Topological constraints enumeration can be precisely evaluated and computed from MD simulations by following doublets or triplets of neighbor atoms over the simulated trajectory to evaluate bonds and angle rigidity respectively. As such, a topological constraint can be identified if the motion of a doublet (or triplet in the case of an angle) is correlated over time. Conversely, if their motion is to high and the considered atoms are no longer first neighbors, no constraints are generated. These information can be quantified by computing the pair or angle distribution from radial and angular motion of a doublet or triplet of atoms. These distributions are characterized by a radial σ_r or angular σ_θ excursion around a mean value for a given doublet or triplet of atoms. As a result, it provides additional structural data and insights about the strength of an underlying BS or BB constraints. A small excursion will be characteristic of an active constraint, whereas a high excursion will define a broken constraint. Detailed calculation methods can be found elsewhere[60,70,85,86].

DATA AVAILABILITY

The data that supports the findings of this study are available from the corresponding author upon reasonable request.

REFERENCES

1. Morse, D. L. & Evenson, J. W. Welcome to the Glass Age. *Int. J. Appl. Glass Sci.* **7**, 409–412 (2016).
2. Smedskjaer, M. M., Youngman, R. E. & Mauro, J. C. Principles of Pyrex®glass chemistry: structure-property relationships. *Appl. Phys. A* **116**, 491–504 (2014).
3. Mauro, J. C., Philip, C. S., Vaughn, D. J. & Pambianchi, M. S. Glass Science in the United States: Current Status and Future Directions. *Int. J. Appl. Glass Sci.* **5**, 2–15 (2014).
4. Ball, P. Concrete mixing for gorillas. *Nat. Mater.* **14**, 472–472 (2015).
5. Oliveira, J. M., Correia, R. N., Fernandes, M. H. & Rocha, J. Influence of the CaO/MgO ratio on the structure of phase-separated glasses: a solid state 29Si and 31P MAS NMR study. *J. Non-Cryst. Solids* **265**, 221–229 (2000).
6. Kokubo, T., Kushitani, H., Ohtsuki, C., Sakka, S. & Yamamuro, T. Chemical reaction of bioactive glass and glass-ceramics with a simulated body fluid. *J. Mater. Sci.: Mater. Med.* **3**, 79–83 (1992).
7. Diba, M., Tapia, F., Boccaccini, A. R. & Strobel, L. A. Magnesium-Containing Bioactive Glasses for Biomedical Applications. *Int. J. Appl. Glass Sci.* **3**, 221–253 (2012).
8. Bellucci, D., Veronesi, E., Dominici, M. & Cannillo, V. A new bioactive glass with extremely high crystallization temperature and outstanding biological performance. *Mater. Sci. Eng. C* **110**, 110699 (2020).
9. Gin, S. et al. An international initiative on long-term behavior of high-level nuclear waste glass. *Mater. Today* **16**, 243–248 (2013).
10. Backhouse, D. J., Corkhill, C. L., Hyatt, N. C. & Hand, R. J. Investigation of the role of Mg and Ca in the structure and durability of aluminoborosilicate glass. *J. Non-Cryst. Solids* **512**, 41–52 (2019).
11. Thien, B. M. J., Godon, N., Ballestero, A., Gin, S. & Ayral, A. The dual effect of Mg on the long-term alteration rate of AVM nuclear waste glasses. *J. Nucl. Mater.* **427**, 297–310 (2012).
12. Vernaz, t & Bruezière, J. History of Nuclear Waste Glass in France. *Procedia Mat. Sci.* **7**, 3–9 (2014).
13. Bechgaard, T. K. et al. Structure of MgO/CaO sodium aluminosilicate glasses: Raman spectroscopy study. *J. Non-Cryst. Solids* **470**, 145–151 (2017).
14. Bradtmuller, H. et al. Structural Origins of Crack Resistance on Magnesium Aluminoborosilicate Glasses Studied by Solid-State NMR. *J. Phys. Chem. C* **123**, 14941–14954 (2019).
15. Mauro, J. C., Tandia, A., Vargheese, K. D., Mauro, Y. Z. & Smedskjaer, M. M. Accelerating the Design of Functional Glasses through Modeling. *Chem. Mater.* **28**, 4267–4277 (2016).
16. Wang, M. Y., Smedskjaer, M. M., Mauro, J. C., Sant, G. & Bauchy, M. Topological Origin of the Network Dilation Anomaly in Ion-Exchanged Glasses. *Phys. Rev. Appl.* **8**, 054040 (2017).
17. Lograd, M., Eckert, H., Murata, T., Nakane, S. & Yamazaki, H. Structure-property relations in crack-resistant alkaline-earth aluminoborosilicate glasses studied by solid state NMR. *J. Am. Ceram. Soc.* **105**, 2250–2267 (2021).
18. Angeli, F. et al. Effect of thermally induced structural disorder on the chemical durability of International Simple Glass. *npj Mat. Deg.* **2**, 31 (2018).
19. Gin, S., Beaudoux, X., Angeli, F., Jégou, C. & Godon, N. Effect of composition on the short-term and long-term dissolution rates of ten borosilicate glasses of increasing complexity from 3 to 30 oxides. *J. Non-Cryst. Solids* **358**, 2559–2570 (2012).
20. Reiser, J. T. et al. Effects of Al:Si and (Al.Na):Si Ratios on the Static Corrosion of Sodium-Boroaluminosilicate Glasses. *Int. J. Appl. Glass Sci. n/a.* **13**, 91–111 (2022).
21. Guo, R., Brigden, C. T., Gin, S., Swanton, S. W. & Farnan, I. The effect of magnesium on the local structure and initial dissolution rate of simplified UK Magnox waste glasses. *J. Non-Cryst. Solids* **497**, 82–92 (2018).
22. Bunker, B. C. Molecular mechanisms for corrosion of silica and silicate glasses. *J. Non-Cryst. Solids* **179**, 300–308 (1994).
23. Vienna, J. D., Neeway, J. J., Ryan, J. V. & Kerisit, S. N. Impacts of glass composition, pH, and temperature on glass forward dissolution rate. *npj Mat. Deg.* **2**, 22 (2018).
24. Jollivet, P., Gin, S. & Schumacher, S. Forward dissolution rate of silicate glasses of nuclear interest in clay-equilibrated groundwater. *Chem. Geol.* **330-331**, 207–217 (2012).
25. Neeway, J. et al. Vapor hydration of SON68 glass from 90 °C to 200 °C: a kinetic study and corrosion products investigation. *J. Non-Cryst. Solids* **358**, 2894–2905 (2012).
26. Inagaki, Y., Kikunaga, T., Idemitsu, K. & Arima, T. Initial Dissolution Rate of the International Simple Glass as a Function of pH and Temperature Measured Using Microchannel Flow-Through Test Method. *Int. J. Appl. Glass Sci.* **4**, 317–327 (2013).
27. Fournier, M., Gin, S. & Frugier, P. Resumption of nuclear glass alteration: State of the art. *J. Nucl. Mater.* **448**, 348–363 (2014).
28. Gin, S. et al. The fate of silicon during glass corrosion under alkaline conditions: a mechanistic and kinetic study with the International Simple Glass. *Geochim. Cosmochim. Acta* **151**, 68–85 (2015).
29. Jollivet, P. et al. Effect of clayey groundwater on the dissolution rate of the simulated nuclear waste glass SON68. *J. Nucl. Mater.* **420**, 508–518 (2012).
30. Ribet, S. & Gin, S. Role of neoformed phases on the mechanisms controlling the resumption of SON68 glass alteration in alkaline media. *J. Nucl. Mater.* **324**, 152–164 (2004).
31. Fleury, B., Godon, N., Ayral, A. & Gin, S. SON68 glass dissolution driven by magnesium silicate precipitation. *J. Nucl. Mater.* **442**, 17–28 (2013).
32. Debure, M., Frugier, P., De Windt, L. & Gin, S. Borosilicate glass alteration driven by magnesium carbonates. *J. Nucl. Mater.* **420**, 347–361 (2012).
33. Frugier, P., Martin, C., Ribet, I., Advocat, T. & Gin, S. The effect of composition on the leaching of three nuclear waste glasses: R7T7, AVM and VRZ. *J. Nucl. Mater.* **346**, 194–207 (2005).
34. Aréna, H. et al. Impact of iron and magnesium on glass alteration: characterization of the secondary phases and determination of their solubility constants. *Appl. Geochem.* **82**, 119–133 (2017).
35. Aréna, H. et al. Impact of Fe, Mg and Ca elements on glass alteration: Interconnected processes. *Geochim. Cosmochim. Acta* **239**, 420–445 (2018).
36. Iwalewa, T. M., Qu, T. & Farnan, I. Investigation of the maximum dissolution rates and temperature dependence of a simulated UK nuclear waste glass in circumneutral media at 40 and 90 °C in a dynamic system. *Appl. Geochem.* **82**, 177–190 (2017).
37. Goût, T. L., Harrison, M. T. & Farnan, I. Evaluating the temperature dependence of Magnox waste glass dissolution. *J. Non-Cryst. Solids* **518**, 75–84 (2019).
38. Harrison, M. T. The Effect of Composition on Short- and Long-term Durability of UK HLW Glass. *Procedia Mater. Sci.* **7**, 186–192 (2014).
39. Cassingham, N. et al. The initial dissolution rates of simulated UK Magnox-ThORP blend nuclear waste glass as a function of pH, temperature and waste loading. *Mineral. Mag.* **79**, 1529–1542 (2015).
40. Bauchy, M. Deciphering the atomic genome of glasses by topological constraint theory and molecular dynamics: a review. *Comput. Mater. Sci.* **159**, 95–102 (2019).
41. Mauro, J. Topological constraint theory of glass. *Am. Ceramic Soc. Bullet.* **90**, 31–37 (2011).
42. Thorpe, M. F. Continuous deformations in random networks. *J. Non-Cryst. Solids* **57**, 355–370 (1983).
43. Phillips, J. C. Topology of covalent non-crystalline solids I: Short-range order in chalcogenide alloys. *J. Non-Cryst. Solids* **34**, 153–181 (1979).
44. Smedskjaer, M. M., Mauro, J. C. & Yue, Y. Prediction of Glass Hardness Using Temperature-Dependent Constraint Theory. *Phys. Rev. Lett.* **105**, 115503 (2010).
45. Zheng, Q., Yue, Y. & Mauro, J. C. Density of topological constraints as a metric for predicting glass hardness. *Appl. Phys. Lett.* **111**, 011907 (2017).
46. Wang, B., Yu, Y., Wang, M., Mauro, J. C. & Bauchy, M. Nanoductility in silicate glasses is driven by topological heterogeneity. *Phys. Rev. B* **93**, 064202 (2016).
47. Bauchy, M. et al. Fracture toughness anomalies: viewpoint of topological constraint theory. *Acta Materialia* **121**, 234–239 (2016).
48. Pignatelli, I., Kumar, A., Bauchy, M. & Sant, G. Topological Control on Silicates' Dissolution Kinetics. *Langmuir* **32**, 4434–4439 (2016).

49. Oey, T. et al. The role of the network-modifier's field-strength in the chemical durability of aluminoborate glasses. *J. Non-Cryst. Solids* **505**, 279–285 (2019).

50. Oey, T. et al. Topological controls on the dissolution kinetics of glassy aluminosilicates. *J. Am. Ceram. Soc.* **100**, 5521–5527 (2017).

51. Mascaraque, N., Bauchy, M. & Smedskjaer, M. M. Correlating the Network Topology of Oxide Glasses with their Chemical Durability. *J. Phys. Chem. B* **121**, 1139–1147 (2017).

52. Mascaraque, N. et al. Dissolution Kinetics of Hot Compressed Oxide Glasses. *J. Phys. Chem. B* **121**, 9063–9072 (2017).

53. Gin, S. et al. Can a simple topological-constraints-based model predict the initial dissolution rate of borosilicate and aluminosilicate glasses? *npj Mat. Deg.* **4**, 6 (2020).

54. Wilkinson, C. J. et al. Topological Origins of the Mixed Alkali Effect in Glass. *J. Phys. Chem. B* **123**, 7482–7489 (2019).

55. Bisbrouck, N. et al. Impact of magnesium on the structure of aluminoborosilicate glasses: a solid-state NMR and Raman spectroscopy study. *J. Am. Ceram. Soc.* **104**, 4518–4536 (2021).

56. Bisbrouck, N. et al. Influence of Magnesium on the Structure of Complex Multicomponent Silicates: insights from Molecular Simulations and Neutron Scattering Experiments. *J. Phys. Chem.* **125**, B11761–11776 (2021).

57. Bauchy, M. et al. Angular rigidity in tetrahedral network glasses with changing composition. *Phys. Rev. B* **84**, 054201 (2011).

58. Bauchy, M., Micoulaut, M., Boero, M. & Massobrio, C. Compositional Thresholds and Anomalies in Connection with Stiffness Transitions in Network Glasses. *Phys. Rev. Lett.* **110**, 165501 (2013).

59. Bauchy, M. & Micoulaut, M. Densified network glasses and liquids with thermodynamically reversible and structurally adaptive behaviour. *Nat. Commun.* **6**, 6398 (2015).

60. Laurent, O., Mantisi, B. & Micoulaut, M. Structure and Topology of Soda-Lime Silicate Glasses: Implications for Window Glass. *J. Phys. Chem. B* **118**, 12750–12762 (2014).

61. Bauchy, M. & Micoulaut, M. Transport Anomalies and Adaptative Pressure-Dependent Topological Constraints in Tetrahedral Liquids: evidence for a Reversibility Window Analogue. *Phys. Rev. Lett.* **110**, 095501 (2013).

62. Devreux, F. & Kolb, M. Kinetics of leaching near the percolation threshold. *J. Non-Cryst. Solids* **242**, 14–18 (1998).

63. Nicoleau, E. et al. Phase separation and crystallization effects on the structure and durability of molybdenum borosilicate glass. *J. Non-Cryst. Solids* **427**, 120–133 (2015).

64. Veléz, M. H., Tuller, H. L. & Uhlmann, D. R. Chemical durability of lithium borate glasses. *J. Non-Cryst. Solids* **49**, 351–362 (1982).

65. Bunker, B. C., Arnold, G. W., Day, D. E. & Bray, P. J. The effect of molecular structure on borosilicate glass leaching. *J. Non-Cryst. Solids* **87**, 226–253 (1986).

66. George, J. *Dissolution of borate glasses and precipitation of phosphate compounds*. Doctoral Dissertations (Missouri University of Science and Technology, 2015).

67. Fiske, P. S. & Stebbins, J. F. The Structural of Mg in Silicate Liquids - a High-Temperature Mg-25, Na-23, and Si-29 NMR-Study. *Am. Mineral.* **79**, 848–861 (1994).

68. Shimoda, K., Tobu, Y., Hatakeyama, M., Nemoto, T. & Saito, K. Structural investigation of Mg local environments in silicate glasses by ultra-high field 25Mg 3QMAS NMR spectroscopy. *Am. Mineral.* **92**, 695–698 (2007).

69. Watts, S. J., Hill, R. G., O'Donnell, M. D. & Law, R. V. Influence of magnesia on the structure and properties of bioactive glasses. *J. Non-Cryst. Solids* **356**, 517–524 (2010).

70. Micoulaut, M. Concepts and applications of rigidity in non-crystalline solids: a review on new developments and directions. *Adv. Phys-X* **1**, 147–175 (2016).

71. Liu, H., Du, T., Krishnan, N. M. A., Li, H. & Bauchy, M. Topological optimization of cementitious binders: advances and challenges. *Cem. Concr. Compos.* **101**, 5–14 (2019).

72. Yang, K. et al. Analytical model of the network topology and rigidity of calcium aluminosilicate glasses. *J. Am. Ceram. Soc.* **104**, 3947–3962 (2021).

73. Yang, K. et al. Prediction of the Young's modulus of silicate glasses by topological constraint theory. *J. Non-Cryst. Solids* **514**, 15–19 (2019).

74. Bauchy, M. Topological Constraints and Rigidity of Network Glasses from Molecular Dynamics Simulations. *American Ceramic Society Bulletin.* **91**, 34 (2012).

75. Mauro, J. C., Gupta, P. K. & Loucks, R. J. Composition dependence of glass transition temperature and fragility. II. A topological model of alkali borate liquids. *J. Chem. Phys.* **130**, 234503 (2009). Publisher: American Institute of Physics.

76. Sreeram, A. N., Swiler, D. R. & Varshneya, A. K. Gibbs-DiMarzio equation to describe the glass transition temperature trends in multicomponent chalcogenide glasses. *J. Non-Cryst. Solids* **127**, 287–297 (1991).

77. Naumis, G. G. Variation of the glass transition temperature with rigidity and chemical composition. *Phys. Rev. B* **73**, 172202 (2006).

78. Damodaran, K., Delaye, J.-M., Kalinichev, A. G. & Gin, S. Deciphering the Non-Linear Impact of Al on Chemical Durability of Silicate Glass. *Acta Materialia.* **225**, 117478, https://doi.org/10.1016/j.actamat.2021.117478 (2022).

79. Hamilton, J. P., Brantley, S. L., Pantano, C. G., Criscenti, L. J. & Kubicki, J. D. Dissolution of nepheline, jadeite and albite glasses: toward better models for aluminosilicate dissolution. *Geochim. Cosmochim. Acta* **65**, 3683–3702 (2001).

80. Zapol, P., He, H., Kwon, K. D. & Criscenti, L. J. First-Principles Study of Hydrolysis Reaction Barriers in a Sodium Borosilicate Glass. *Int. J. Appl. Glass Sci.* **4**, 395–407 (2013).

81. Gin, S., Delaye, J.-M., Angeli, F. & Schuller, S. Aqueous alteration of silicate glass: state of knowledge and perspectives. *npj Mater Degra.* **5**, 1–20, https://doi.org/10.1038/s41529-021-00190-5 (2021).

82. Fournier, M. et al. Glass dissolution rate measurement and calculation revisited. *J. Nucl. Mater.* **476**, 140–154 (2016).

83. Plimpton, S. Fast Parallel Algorithms for Short-Range Molecular-Dynamics. *J. Comput. Phys.* **117**, 1–19 (1995).

84. Wang, M. et al. A new transferable interatomic potential for molecular dynamics simulations of borosilicate glasses. *J. Non-Cryst. Solids* **498**, 294–304 (2018).

85. Bauchy, M., Abdolhosseini Qomi, M. J., Bichara, C., Ulm, F.-J. & Pellenq, R. J.-M. Nanoscale Structure of Cement: Viewpoint of Rigidity Theory. *J. Phys. Chem. C* **118**, 12485–12493 (2014).

86. Micoulaut, M., Bauchy, M. & Flores-Ruiz, H. Topological Constraints, Rigidity Transitions, and Anomalies in Molecular Networks. In *Molecular Dynamics Simulations of Disordered Materials: from Network Glasses to Phase-Change Memory Alloys*, 275–311 (Springer, Cham, 2015).

AUTHOR CONTRIBUTIONS

N.B. wrote the paper and performed the leaching experiments. N.B. and M.M. performed the TCT calculation and analyses. F.A., S.G., and J-M.D. supervised the study. All the authors helped on the paper editing.

COMPETING INTERESTS

The authors declare no competing interests.

ADDITIONAL INFORMATION

Correspondence and requests for materials should be addressed to F. Angeli.

Reprints and permission information is available at http://www.nature.com/reprints

Publisher's note Springer Nature remains neutral with regard to jurisdictional claims in published maps and institutional affiliations.